Journal of Materials Chemistry A

Accepted Manuscript

ROYAL SOCIETY OF CHEMISTRY

www.rsc.org/materialsA

Journal Name

ARTICLE

Visible-light-driven photocatalytic bacterial inactivation and mechanism of zinc oxysulfide under LED light irradiation

Received 00th January 20xx,
Accepted 00th January 20xx

DOI: 10.1039/x0xx00000x

www.rsc.org/

Dan Wu, [a] Wei Wang, [a,b,*] Tsz Wai Ng, [a] Guocheng Huang, [a] Dehua Xia, [a] Ho Yin Yip, [a] Hung Kay Lee [c] Guiying Li[d], Taicheng An[d] and Po Keung Wong [a,*]

Zinc oxysulfide ($ZnO_{0.6}S_{0.4}$) nanoparticles, prepared via a coprecipitation-calcination method, were firstly used as an effective visible-light-driven (VLD) photocatalyst for inactivation of a typical Gram-negative bacterium, *Escherichia coli* K-12. Energy-saving white light emitting diode (LED) lamp was employed as the visible light (VL) source. Compared to only UV-responsive pure ZnO and ZnS, the light active region of $ZnO_{0.6}S_{0.4}$ was expanded as far as 550 nm in the VL region. Significantly, the obtained $ZnO_{0.6}S_{0.4}$ nanoparticles showed considerable VLD photocatalytic bacterial inactivation activity under white LED irradiation. The mechanism of inactivation was investigated in-depth. Photogenerated holes (h^+) and hydrogen peroxide (H_2O_2) were predominantly responsible for the bacterial inactivation. Moreover, H_2O_2 was evidenced only from the derivation of electrons in conduction band of $ZnO_{0.6}S_{0.4}$ in the present photocatalytic system. The integrated damage from the direct oxidation effect of h^+ and continuous accumulation of H_2O_2 resulted in the high bacterial inactivation efficiency of $ZnO_{0.6}S_{0.4}$ nanoparticles under visible white LED lamp irradiation. The destruction process of bacterial cell by $ZnO_{0.6}S_{0.4}$ photocatalyst was also monitored to begin from the attack of cell membrane and then to the release of intracellular components.

Introduction

The emergence of pathogenic bacteria in surface water poses serious threats to public health worldwide, which commonly cause infectious waterborne diseases in human. [1] Thus, it is of great importance to develop effective disinfection strategies for adequate inactivation of pathogenic microorganisms in water body. In recent years, semiconductor photocatalysis has attracted growing interest as a promising technique for removal of bacterial contaminations owing to its powerful photocatalytic ability. [2, 3] As important II-VI semiconductors, zinc oxide (ZnO) and zinc sulfide (ZnS) have been intensively studied due to numerous advantages of low cost, earth-abundance, low toxicity and marked photocatalytic performance. [4-6] Unfortunately, both ZnO and ZnS process a large band gap (3.4 and 3.7 eV for ZnO and ZnS, respectively), thus can only response to ultraviolet (UV) light, which severely limits their practical applications in the cases of UV shortage. Furthermore, the UV light only contributes to about 4% of solar energy and the VL accounts for about 43%, [7] while ordinary indoor lighting is also dominated by VL. [8] Additionally, long-time exposure to bio-hazardous UV light also brings adverse health impacts on humans. Therefore, efficient utilization of VL or sun light energy is of significance for implementing photocatalysis in indoor and outdoor environment, respectively.

As a consequence, it is highly desirable to engineer ZnO and ZnS with improved VL responsiveness. In this respect, the conventional technique is impurity doping. [9] Nevertheless, in the cases of ZnS and ZnO, this approach is limited by the maximum doping ability [10] and low mobility of photogenerated electrons and holes. [11] An interesting alternative is to couple ZnO and ZnS into nanoarchitectures with multilayered structures, core/shell heterostructures and solid solutions. [12-15] For example, Bao *et al.* prepared ZnO/ZnS heterostructured nanorods arrays with hydrogen (H_2) production of 19.2 mmol h^{-1} for 0.05 g catalyst under solar-simulated light irradiation. [13] Rai *et al.* fabricated an efficient and highly sensitive UV/VL photodetector based on ZnO/ZnS core/shell nanowires. [14] Lahiri *et al.* found that surface functionalization of ZnO photocatalysts with monolayer ZnS resulted in an effective surface band gap narrowing to 2.8 eV. [15] In particular, composition controlled ternary zinc nanostructure, named zinc oxysulfide (ZnOS), has recently been explored due to feasible bandgap engineering in a wide range. [16, 17] Because of the

[a] School of Life Sciences and [c] Department of Chemistry, The Chinese University of Hong Kong, Shatin, NT, Hong Kong SAR, China. Tel: +852-39436383, Fax: +852-26035767, E-mail: pkwong@cuhk.edu.hk.
[b] State Key Laboratory of Material Processing and Die & Mould Technology, Huazhong University of Science and Technology, Wuhan 430074, China. Tel: +86-87541540, Fax: +86-87541540, E-mail: weiwang@hust.edu.cn
[d] Guangzhou Institute of Geochemistry, Chinese Academy of Sciences, Guangzhou 510640, China. Tel: +86-20-8529 1501, Fax: +86-20-8529 0706, E-mail: antc99@gig.ac.cn

† Electronic Supplementary Information (ESI) available. See DOI: 10.1039/x0xx00000x

staggered type-II band alignment [18] and the hybrid orbitals of oxygen (O) and sulfur (S) caused by the formation of an oxysulfide, [19, 20] the band gap of ZnOS could be much smaller than either of the individual components. Expectedly, Pandey *et al.* synthesized a series of ZnOS semiconductors with various O/S molar ratios and found that $ZnO_{0.6}S_{0.4}$ had the narrowest bandgap of 2.7 eV. [17, 21] Thus, owing to the large difference of atomic radius and electron-negativities between O and S atom, the formation of ZnOS would consequently bring dramatically changes in its electrical and optical properties, [20] leading to extended photo-response and the narrowing photoexcitation threshold energy. Accordingly, ZnOS photocatalysts would exhibit improved photocatalytic activity under VL irradiation. [11, 19, 20, 22] However, all previous studies about photocatalytic performance of ZnOS only focused on hydrogen production [20, 22] and dye degradation. [11, 19] To the best of our knowledge, VLD photocatalytic bacterial inactivation by ZnOS nanostructures has never been explored. Moreover, the underlying bacterial inactivation mechanism of ZnOS photocatalysts under pure VL irradiation has never been attempted in detail.

Additionally, conventional indoor VL sources including the fluorescent and incandescent lights are widely used in common life. However, they suffer from disadvantages of mercury-containing, high cost and energy consumption. [8] In contrast, as a kind of energy efficient VL source, white light emitting diode (LED) lamp serves as a promising alternative to efficient utilization of VL in indoor environment. Compared with traditional light sources, LED lamp offers various advantages of a longer life time, a higher electricity-to-light yield with little heating and a lower energy consumption, suitable operation in a pulsed regime at high frequencies, and being a green mercury-free radiation source with an almost complete recycling. [8, 23] Besides, using LED lamp provides not only the pure VL, but also the opportunity to develop system miniaturized and configuration flexible equipment. [24]

In this work, zinc oxysulfide ($ZnO_{0.6}S_{0.4}$) nanoparticles as VLD photocatalysts were achieved via a simple coprecipitation-calcination method. The crystal structure, optical property, and electronic structure of as-prepared $ZnO_{0.6}S_{0.4}$ nanoparticles were systemically investigated. For the first time, the photocatalytic activities of obtained $ZnO_{0.6}S_{0.4}$ nanoparticles were evaluated by inactivation of a Gram-negative bacterium, *Escherichia coli* K-12, under visible white LED lamp irradiation. Moreover, the VLD photocatalytic bacterial inactivation mechanism was systemically explored. The major reactive species involved in the bacterial inactivation process were also identified.

Experimental

Preparation of zinc oxysulfide

Zinc oxysulfide (ZnOS) was prepared through a coprecipitation-calcination method. In brief, 2.98 g of $Zn(NO_3)_2{\cdot}6H_2O$ and 0.1 g of $Na_3C_6H_5O_7{\cdot}5.5H_2O$ were dissolved in 50 mL of distilled water. An aqueous solution containing 0.48 g of NaOH and 0.96 g of $Na_2S{\cdot}9H_2O$ was added dropwise into the above zinc ion solution under stirring. After continuous stirring for another 2 h at room temperature (*ca.* 25 °C), the precipitate was washed with distilled water and ethanol several times, respectively. After being dried at 50 °C for 12 h, the precipitate was calcined at 400 °C for 2 h in argon (Ar) flow to obtain ZnOS nanoparticles. For comparison, pure ZnO and ZnS samples were also prepared using a similar procedure as above mentioned, except only using NaOH (0.8 g) and $Na_2S{\cdot}9H_2O$ (2.4 g) as precipitation agent, respectively. All the chemicals used in the experiments were of reagent grade and used as received without further purification.

Characterizations

X-ray diffraction (XRD) patterns were recorded on a Bruker D8 advance diffractometer operating at 40 mA and 40 kV using Cu Kα as radiation source. Transmission electron microscopic (TEM) analysis was conducted using a Tecnai G2 Spirit transmission electron microscope at 200 kV. Morphology and elemental composition of the products were analyzed by scanning electron microscopy (SEM, FEI/Nova NanoSEM 450) equipped with an energy-dispersive X-ray (EDX) analyzer (Oxford/X-Max 50). UV-vis diffuse reflectance spectra (UV–vis DRS) were measured with a Varian Cary 500 UV-vis spectrophotometer equipped with a labsphere diffuse reflectance accessory and BaSO4 was used as a reflectance standard. X-ray photoelectron spectroscopy (XPS) measurements were conducted on an AXIS-ULTRA DLD-600W X-ray photoelectron spectrometer using Al-Kα radiation as excitation source. Fourier transform infrared (FTIR) spectra were measured using a Nicolet 670 FTIR spectrometer (Thomas Nicolet, Waltham, USA). Electron paramagnetic resonance (EPR) spectra were recorded on an EMX EPR spectrometer (Bruker, Karlsruhe, Germany).

Photocatalytic inactivation activity

The photocatalytic inactivation activity of the samples was evaluated by the inactivation of *Escherichia coli* K-12 (*E. coli*). The white Light-emitting-diode (LED) lamps (10 W, Philips) with light intensity of 15 mW/cm^2 were used as the light source. The light spectrum of LED lamps was shown in Fig. S1. The cells of *E. coli* K-12 were inoculated into 50 mL of nutrient broth (Lab M, Lancashire, UK) and incubated at 37 °C for 15 h in a shaking incubator. The bacterial cells were harvested by centrifugation for 1 min and then washed twice with sterilized saline (0.9 % NaCl). Finally the cell pellet was re-suspended in sterilized saline. The final cell density was adjusted to about 1×10^7 colony forming unit (CFU)/mL. Before irradiation, the suspension (50 mL) containing the bacterial cells and the photocatalyst (20 mg) was under continuous stirring for 0.5 h in dark to reach the adsorption equilibrium. At different time intervals, an aliquot of the reaction mixture was collected, serially diluted with sterilized saline solution and plated on Nutrient Agar. The number of colonies was counted after incubating at 37 °C for 24 h. All of the above experiments were conducted in triplicates. The data shown are the average of triplicates and error bars represent the standard deviation.

The bacterial cells were stained with a LIVE/DEAD BacLight Bacterial Viability Kit (L7012, Molecular Probes, Inc., Eugene, USA) following the procedure recommended by the

manufacturer. The samples were examined under an ECLIPSE 80i fluorescence microscope (Nikon, Tokyo, Japan) equipped with a filter block NUV-2A consisting of excitation filter Ex 400-680 (Nikon, Tokyo, Japan) and Spot-K slider CCD camera (Diagnostic Instruments Inc., Sterling Heights, USA).

Results and discussion

Characterizations of the synthesized photocatalyst

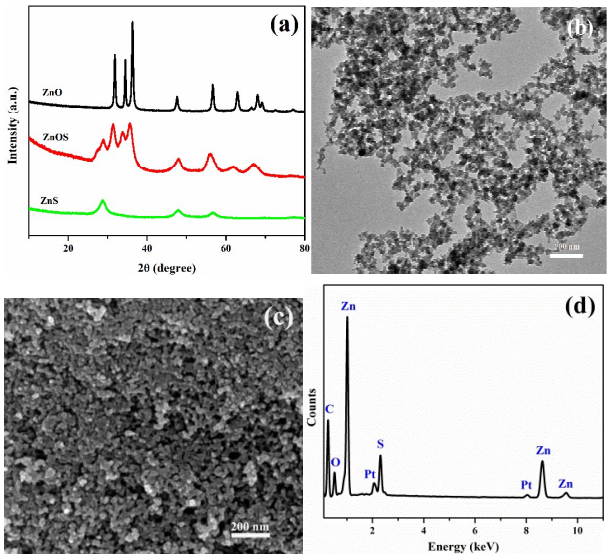

Fig. 1 (a) XRD patterns of as-prepared samples and (b) TEM image (c) SEM image (d) EDX of ZnOS.

Fig. 1a illustrates comparative XRD patterns of ZnO, ZnS, and ZnOS samples. All diffraction peaks of as-prepared ZnO and ZnS samples can be well indexed to a hexagonal wurtzite structure ZnO (JCPDS 01-070-2551) and a cubic blende structure ZnS (JCPDS 96-500-0089), respectively. Clearly, two sets of diffraction peaks were observed in ZnOS samples, where the peaks at 2θ= 31.5°, 33.8°, 35.7°, 61.7° and 67.1° corresponded to the (100), (002), (101), (103) and (200) planes of ZnO, respectively, while the peaks at 28.9°, 47.9 and 56.1° corresponded to the (111), (022) and (113) planes of ZnS, respectively. However, only partial diffraction peaks can be found and there was some angle shift in ZnOS samples compared to pure ZnO and ZnS. Besides, only two bumps appeared in the XRD pattern of the ZnOS precursor before calcination (Fig. S2), which suggested that the product before calcination were of amorphous phases [25-27] and the subsequent thermal treatment resulted in the $ZnO_{0.6}S_{0.4}$ products of crystalline phases. Consequently, the results demonstrated that ZnOS samples were not a simple mixture of ZnO and ZnS. Notably, the broader diffraction peaks of ZnOS were observed, which was ascribed to the mismatch between O and S in the ZnOS lattice. [28] Fig. 1b presents the TEM image of ZnOS samples. It was clearly observed that the size of $ZnO_{0.6}S_{0.4}$ nanoparticles was about 5–20 nm. The SEM image (Fig. 1c) further confirmed the nanostructure of ZnOS with many tightly aggregated small nanoparticles. A typical EDX spectrum (Fig. 1d) exhibits the presence of Zn, O, and S elements, indicating that the obtained ZnOS nanoparticles were of high purity. Moreover, uniform distributions of these respective elements in the compositional architecture of ZnOS nanoparticles were further shown in corresponding EDX mappings (Fig. S3). Thus, we reasonably speculated that Zn should have chemical bonding to both S and O elements in the lattice of ZnOS nanoparticles.

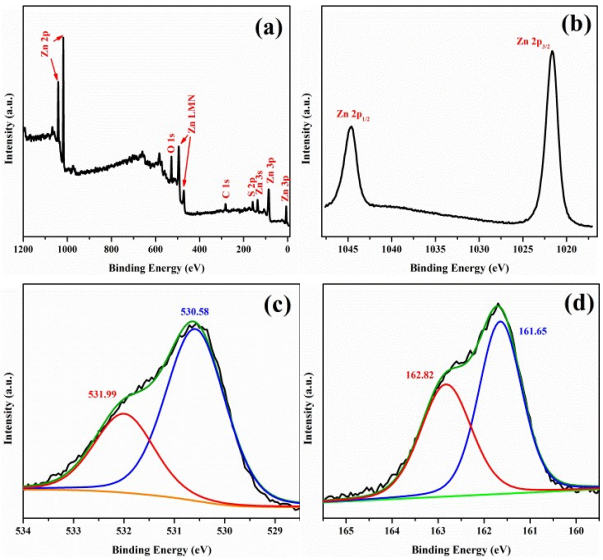

Fig. 2 XPS spectra of (a) survey scan, (b) Zn 2p, (c) O 1s and (d) S 2p for $ZnO_{0.6}S_{0.4}$ nanoparticles.

The purity and element composition of the $ZnO_{0.6}S_{0.4}$ nanoparticles were further analyzed by XPS. Apart from the C element, all of the peaks on the scan survey spectra (Fig. 2a) can be ascribed to Zn, O and S elements, further validating the high purity of ZnOS nanoparticles. As shown in Fig. 2b, the symmetric peaks located at the binding energies (BE) of 1044.64 and 1021.69 eV corresponded to Zn $2p_{1/2}$ and Zn $2p_{3/2}$, respectively, which indicated that Zn existed in the form of Zn^{2+} chemical state in ZnOS. Fig. 2c shows the asymmetric O 1s peak for ZnOS, which can be deconvoluted into two peaks. The lower peak centered at BE of 530.58 eV can be ascribed to the lattice O atoms coordinated with Zn atoms, while the peak located at higher BE of 531.99 eV was due to the adsorbed oxygen species on ZnOS surface. [29] Considering that the photocatalysis takes place on the surfaces of semiconductors, the absorbed oxygen species are easily captured by photogenerated electrons to form reactive species, contributing to the enhanced photocatalytic properties. [30] The XPS spectra of S 2p in Fig. 2d can be fitted into two peaks locating at BE of 161.65 and 162.82 eV, which was attributed to S $2p_{3/2}$ and S $2p_{1/2}$, respectively, verifying the existence of S^{2-} chemical state in ZnOS nanoparticles. It is worth noting that the absence of a peak related to sulfate species at about BE of 168 eV [31, 32] suggested that Zn atoms was chemically bonded to both S and O atoms in the ZnOS lattice. In addition, the atomic molar ratio of O to S determined by XPS was 1.52, which was highly consistent with theoretical value (0.6:0.4 =

1.5). As aforementioned, the S and O were evidenced to be mismatched in the lattice and the Zn was both chemically bonded with S and O of the final product. In conjunction with the molar ratio determined by XPS, the obtained ZnOS product was named $ZnO_{0.6}S_{0.4}$. All the results demonstrated that $ZnO_{0.6}S_{0.4}$ nanoparticles, rather than a simple mixture of pure ZnO and ZnS, were successfully prepared with high purity.

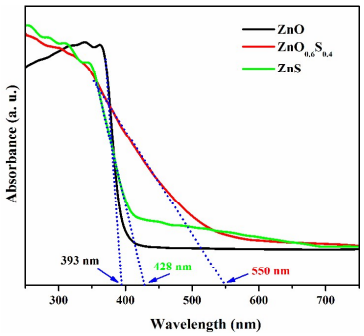

Fig. 3 UV-vis diffuse reflectance spectra (DRS) of ZnO, ZnS and $ZnO_{0.6}S_{0.4}$ nanoparticles.

Fig. 3 presents the UV-vis DRS spectra of the prepared ZnO, ZnS and $ZnO_{0.6}S_{0.4}$ samples. A sharp basal absorption edge for ZnO located at 393 nm, while the main absorption edge of the pure ZnS moved up at about 428 nm. Comparatively, the absorption cutoff wavelength of $ZnO_{0.6}S_{0.4}$ nanoparticles determined by the steep absorption occurred at about 550 nm, suggesting that the present $ZnO_{0.6}S_{0.4}$ photocatalyst were responsive to VL region. Particularly, the band edge of $ZnO_{0.6}S_{0.4}$ was significantly blurred, indicating that the electronic structure of the $ZnO_{0.6}S_{0.4}$ semiconductor was totally different from those of ZnO and ZnS. [16] The band gap energy (E_g) of semiconductors can be estimated based on the Kubelka–Munk function [33] by fitting the absorption band edge of the spectra as $\alpha h\nu = A(h\nu - E_g)^{n/2}$ where α, h, ν, A are the absorption coefficient, Plank constant, the incident light frequency and a constant, respectively. Accordingly, the band gap values were calculated to be 3.16, 2.90 and 2.25 eV corresponding to ZnO, ZnS and $ZnO_{0.6}S_{0.4}$, respectively. The narrowing band gap of $ZnO_{0.6}S_{0.4}$ can be assigned to the atomic orbital coupling of S with O in the valence band of $ZnO_{0.6}S_{0.4}$ semiconductors. [20] Thus, the above results revealed that due to the large differences between the electron-negativities and sizes for S and O atoms, the $ZnO_{0.6}S_{0.4}$ nanoparticles can greatly reduce the band gap and broaden light absorption to VL region. Therefore, the $ZnO_{0.6}S_{0.4}$ nanoparticles were expected to exhibit enhanced photocatalytic activities under VL irradiation compared to that of pure ZnO and ZnS.

VLD photocatalytic bacterial inactivation activity

The photocatalytic performance of $ZnO_{0.6}S_{0.4}$ nanoparticles was evaluated by inactivation of a representative microorganism, *E. coli* K-12, using white LED lamp as the VL source. In dark and light control experiments, the bacterial population remained almost unchanged even after 3 h, indicating no toxic effects of $ZnO_{0.6}S_{0.4}$ nanoparticles to *E. coli* K-12 cells and also no photolysis of bacterial cells under white LED lamp irradiation alone (Fig. 4). Upon visible LED irradiation, no reduction and only slight decrease (about 1-log) of bacterial cells for ZnS and ZnO were observed, respectively. In contrast, the $ZnO_{0.6}S_{0.4}$ nanoparticles showed remarkable enhanced photocatalytic activity for inactivating *E.*

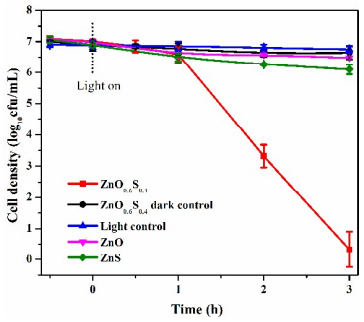

Fig. 4 Photocatalytic bacterial inactivation of *E. coli* K-12 in the presence of ZnO, ZnS and $ZnO_{0.6}S_{0.4}$ under visible LED irradiation.

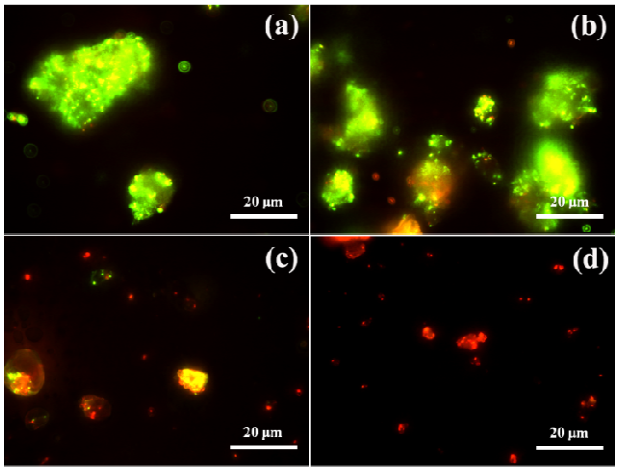

Fig. 5 Fluorescence microscopic images of *E. coli* K-12 photocatalytically treated by $ZnO_{0.6}S_{0.4}$ nanoparticles under visible LED irradiation for (a) 0, (b) 1, (c) 2, and (d) 3 h.

coli K-12, with the complete inactivation of cell densities of 7-log after 3 h of irradiation. On one hand, the white LED lamps used in the present system possess a broad light spectrum only in the VL region ranging from 400 to 800 nm (Fig. S1). On the other hand, in principle, the photocatalysts can only be driven by light of energy is higher than the bandgap energy of semiconductor. Based on the optical properties (Fig. 3), $ZnO_{0.6}S_{0.4}$, ZnO and ZnS can only use the light of wavelength less than 550, 428 and 393 nm, respectively. Accordingly, the different photocatalytic behaviors of these samples were observed. Furthermore, recycle tests of photocatalytic

bacterial inactivation were performed to study the stability of the $ZnO_{0.6}S_{0.4}$ photocatalyst. As shown in Fig. S4, a slight decrease of the inactivation efficiency was observed, mainly due to the accumulation of released substances of bacteria upon inactivation. Additionally, there were no obvious changes about the morphology of $ZnO_{0.6}S_{0.4}$ after each run in the recycling test (Fig. S5), indicating that the photocatalyst is quite stable. Hence, a reasonable conclusion can be drawn that the $ZnO_{0.6}S_{0.4}$ nanoparticles were a kind of true VLD photocatalyst, which can present excellent photocatalytic bacterial inactivation activity.

In order to confirm the bactericidal effect of $ZnO_{0.6}S_{0.4}$ nanoparticles under white LED lamp irradiation, the BacLight kit fluorescent microscopic method was carried out. [34] When the cells were stained with the dye mixtures of membrane-permeable SYTO 9 and membrane-impermeable propidium iodide (PI), dead bacterial cells with damaged cell membranes are stained fluorescent red, whereas live bacterial cells with intact cell membranes are therefore stained fluorescent green. As shown in Fig. 5a, the viable cells expectedly exhibited intense green fluorescence. It is also worth noting that the living bacteria aggregated in a green bulk, which was mainly attributed to the adsorption between abundant small-sized $ZnO_{0.6}S_{0.4}$ nanoparticles and bacterial cells. After being irradiated under white LED lamp for 1 h, some cells stained fluorescent red by PI (Fig. 5b), indicating partial bacteria were cracked under photocatalytic treatment. With prolonged irradiation time, fewer and no living bacteria were further observed after 2 and 3 h, respectively (Fig. 5c and 5d). More information can also be found in Fig. S6. As a solid method to tracing the changes in cell membrane integrity, the fluorescence microscopic results suggested that the cell membrane undergone a progressive damage during the photocatalytic process, resulting release of intracellular components and subsequent cell death.

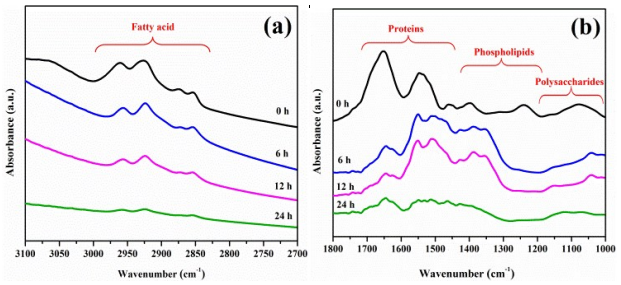

Fig. 6 FTIR spectra of photocatalytically treated baterial cells at different irradiation times. (a) bands in the spectral region ranging from 3100 to 2700 cm^{-1} and (b) bands in the spectral region ranging from 1800 to 1000 cm^{-1}.

The changes in cell structure and functionality induced by photocatalytic treatment were further evidenced by FTIR method. As shown in Fig. 6a, the peak at around 3600 cm^{-1} was attributed to amide B, while the characteristic peaks between 3100 and 2800 cm^{-1} were assigned to C–H stretching vibrations of $-CH_2$ and $-CH_3$ groups which were mainly from fatty acid. [35] Because the cell membrane is predominantly composed of these bonds, the peaks in this region can be employed to track the changes in cell membrane integrity. With prolonged reaction time, the integral absorbance of initial *E. coli* K-12 spectral profile and its corresponding intensity quickly decayed, suggesting photocatalytic damage to the cell membrane. Furthermore, significant decay and disappearance of oligosaccharide bands at around 1080 cm^{-1} was also observed in Fig. 6b, implying the breakdown of polysaccharides with the photocatalytic treatment. As polysaccharides are the dominant surface features of the outer membrane of Gram-negative bacteria, their changes further confirmed the progressive damage to cell membrane. In parallel, longer treatment times also led to significant changes in the profile of PO_2^- near 1243 cm^{-1}, which was indicative to the photocatalytical destruction of phospholipids. [35, 36] Concomitantly, two new peaks at 1390 and 1350 cm^{-1} were detected after 6 h and 12 h and then disappeared after 24 h, resulting from the formation of the intermediates during the breakdown of initial biomolecules and the appearance of C–O stretching bonds during the formation of smaller carboxylic groups in photocatalysis. [37] The region from 1700 to 1500 cm^{-1} was related to the typica bands of proteins, where the peak at 1650 cm^{-1} was attributable to C–O stretching vibrations of amide I band and the peak at 1550 cm^{-1} was specific to N–H bending vibrations of amide II band. [37] The decrease of these peaks indicated the peroxidation of proteins during the photocatalytic process. Although there were some disturbance peaks of $ZnO_{0.6}S_{0.4}$ nanoparticles (Fig. S7), the results reasonably demonstrated that the bacteria were inactivated from initial decomposition of cell membrane and then release and breakdown of intracellular substances in the photocatalytic oxidation process, finally resulting in a cell death.

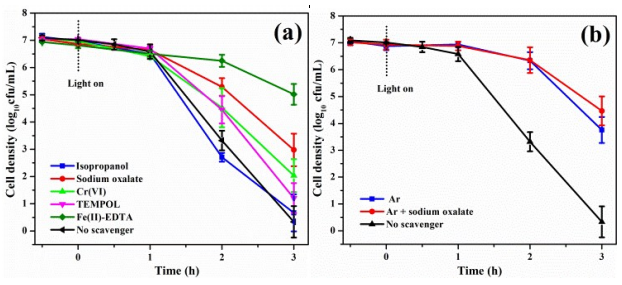

Fig. 7 (a) The photocatalytic inactivation of *E. coli* K-12 using $ZnO_{0.6}S_{0.4}$ nanoparticles as photocatalyst under visible LED irradiation in the presence of different scavengers (no scavenger, 5 mM isopropanol, 2 mM TEMPOL, 0.5 mM sodium oxalate, 0.05 mM Cr(VI), 0.1 mM Fe(II)-EDTA and) in (a) aerobic and (b) anaerobic (Ar purging) conditions.

Photocatalytic inactivation mechanism

To investigate the photocatalytic inactivation mechanism, the scavenger study, which using different reagent individually to remove the specific reactive species, was conducted to systematically explore the roles of various reactive species responsible for the photocatalytic inactivation of the bacteria. The employed concentrations of each scavenger were pre-optimized to achieve their maximum quenching effect but not cause toxicity to bacterial cells. As shown in Fig. 7a, the addition of isopropanol as a scavenger of hydroxyl radical (•OH) had no observable difference in the inactivation efficiency compared to that without scavenger addition, indicating that •OH played neglectable effect on the bacterial inactivation. Meanwhile, with the addition of Cr(VI) and TEMPOL as a scavenger of electron (e^-) and superoxide ($•O_2^-$), respectively, no significant changes in the inactivation efficiency were observed, implying that both e^- and $•O_2^-$ were not the major reactive species accounting for the inactivation of *E. coli*. It was found that the addition of sodium oxalate as a scavenger of hole (h^+) can considerably suppress the bacterial inactivation, which suggested the importance of photogenerated h^+ in the photocatalytic inactivation. Significantly, the major role of hydrogen peroxide (H_2O_2) was also confirmed by a great decrease in the inactivation efficiency after adding Fe(II)-EDTA as a scavenger of H_2O_2. With argon (Ar) purging to remove oxygen, the inactivation efficiency decreased greatly (Fig. 7b). This was attributed to the elimination of H_2O_2 generation pathway from e^- in conduction band (CB), thus only leaving the function of h^+ in valence band (VB). Comparatively, the inactivation only had slight change when adding sodium oxalate in the case of Ar aeration. The result suggested that the major contribution of H_2O_2 was probably from CB. Additionally, the bacterial inactivation kinetics was found to be well fitted with a "shoulder + log-linear" model (Fig. S8) with the parameters of shoulder length (S_L) and inactivation rate (k_{max}). A shoulder length can be considered as cumulative damage period induced by the photocatalytic reactions before the proliferation of a single cell is inhibited. [38] In the case of Ar aeration, the calculated k_{max} (6.25±0.17 h^{-1}) was smaller than that without Ar (7.34±0.31 h^{-1}), suggesting that H_2O_2 derived from CB made important contributions to the bacterial inactivation. Meanwhile, the calculated S_L (1.84±0.03) for inactivation with Ar purging was double than that without Ar (0.90±0.08), which meant that the time to produce a minimum number of radicals inhibiting the bacterial cells proliferation was much longer than the case without Ar. This was ascribed to a rather limited contact of h^+ with the bacterial cells, which only remains on the surface of the photocatalysts and cannot diffuse into the reaction solution. Based on the above results, both H_2O_2 and h^+ were suggested as the dominant effective reactive species responsible for the photocatalytic inactivation of $ZnO_{0.6}S_{0.4}$ nanoparticles.

To further understand the underlying intrinsic mechanism, it is also of significance to locate the positions of the conduction-band minimum (CBM) and the valence-band maximum (VBM) of $ZnO_{0.6}S_{0.4}$ nanoparticles. The band edges of $ZnO_{0.6}S_{0.4}$ nanoparticles were measured by valence-band XPS spectra, as shown in Fig. 8a. The $ZnO_{0.6}S_{0.4}$ nanoparticles presented a VBM energy potential (E_{VB}) at about 1.85 eV. The CBM energy potential (E_{CB}) can be determined by $E_{CB} = E_{VB} - E_g$,

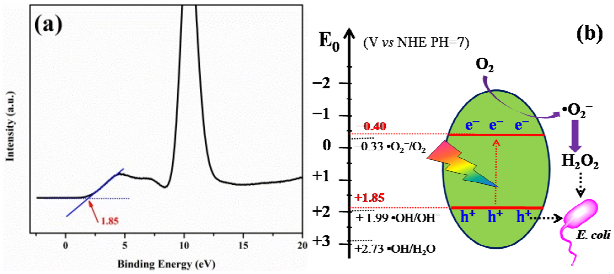

Fig. 8 (a) Valence band XPS spectra and (b) band positions and proposed photocatalytic mechanism of $ZnO_{0.6}S_{0.4}$ nanoparticles.

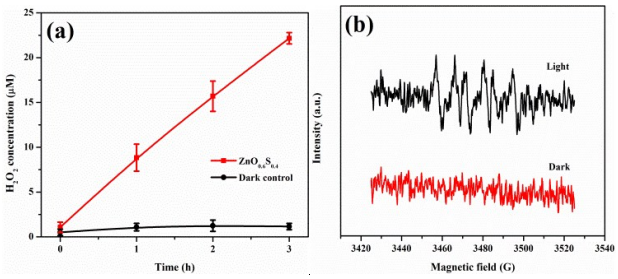

Fig. 9 (a) H_2O_2 produced and (b) EPR spectra of DMPO−OOH generated by $ZnO_{0.6}S_{0.4}$ nanoparticles before and after under visible LED irradiation.

where E_g is the band gap energy. According to the optical adsorption spectrum in Fig. 3, the E_{CB} was calculated to be about −0.40 eV. Therefore, the electronic potentials of CBM and VBM for $ZnO_{0.6}S_{0.4}$ nanoparticles can be determined as displayed in Fig. 8b. The standard redox potentials for $•OH/OH^-$ and $•OH/H_2O$ were reported to located at +1.99 and +2.73 eV, respectively. [33, 34] As a result of more negative E_{VB} (1.85 eV), the photoexcited h^+ in VB of $ZnO_{0.6}S_{0.4}$ cannot oxidize ambient OH^- or H_2O to form •OH, as agreed with the neglectable role of •OH in the scavenger study. Moreover, the absence of •OH was also evidenced through the terephthalic acid fluorescence probe method. It is well known that •OH can react with terephthalic acid in alkaline condition to produce highly fluorescent product, 2-hydroxyterephthalic acid (TAOH) at room temperature, which gives emission at 425 nm with excitation at 315 nm. As shown in Fig. S9, large amounts of •OH was detected in the usual TiO_2-UV photocatalytic system. Comparatively, no detectable fluorescent signals associated with TAOH were found upon visible LED irradiation both in aerobic and anaerobic conditions, further confirming that the generation of •OH was thermodynamically prohibited in present system. Noted that although the energy of h^+ in VB of $ZnO_{0.6}S_{0.4}$ was not high enough to produce •OH, the powerful h^+ can directly attack bacteria cells in photocatalytic oxidation process, [33, 39] which was also validated by the scavenger study.

On the other hand, the standard redox potential for $O_2/\bullet O_2^-$ was about −0.33 eV. Thus, in CB, the photo-generated e^- can be trapped by ambient oxygen to produce reactive $\bullet O_2^-$. Taking account of the production inability of •OH from h^+ in VB, the H_2O_2 was inevitably derived from $\bullet O_2^-$ in CB of $ZnO_{0.6}S_{0.4}$. In fact, the amount of H_2O_2 increased almost linearly with irradiation time and reached as high as 23 μmol after 3 h irradiation (Fig. 9a). The existence of $\bullet O_2^-$ was further verified by the EPR measurements using 5,5-dimethyl-1-pyrroline N-oxide (DMPO) as a spin-trap agent. As shown in Fig. 9b, no resonance signals were observed in dark. Under white LED lamp irradiation, $ZnO_{0.6}S_{0.4}$ nanoparticles displayed a measurable characteristic signal for the DMPO−OOH spin adduct, [40, 41] validating the generation of $\bullet O_2^-$ in the photocatalytic process. In addition, no DMPO−•OH signal was detected, which excluded the presence of •OH in the system, in agreement with above results.

Conclusions

In summary, zinc oxysulfide ($ZnO_{0.6}S_{0.4}$) nanoparticles with enhanced VLD photocatalytic activity were prepared via a coprecipitation-calcination method. Compared to only UV-responsive pure ZnO and ZnS, the light active region of $ZnO_{0.6}S_{0.4}$ was expanded up to 550 nm. Significantly, the obtained $ZnO_{0.6}S_{0.4}$ nanoparticles showed considerable efficiency in photocatalytic inactivating a Gram-negative bacterium, *Escherichia coli* K-12 under visible white LED lamp irradiation, because of a wide VL absorption and suitable band structure. The inactivation kinetics can be well fitted with the typical "shoulder + log-linear" model. The destruction process of bacterial cell by $ZnO_{0.6}S_{0.4}$ photocatalyst was also monitored from the attack of cell membrane to the release of intracellular components. The results of mechanism study indicated that H_2O_2 and photogenerated h^+ were predominantly responsible for the bacterial inactivation. H_2O_2 was suggested from the derivation of e^- in CB of $ZnO_{0.6}S_{0.4}$ in the present photocatalytic system.

Acknowledgements

The research was supported by General Research Fund (GRF14100115) from Research Grant Council and ITSP Tier 3 Scheme (ITS/216/14) from Innovation Technology Commission of Hong Kong SAR Government. The work is also partially supported by National Science Foundation of China (41573086 and 41425015) to G.Y. Li and T.C. An. The authors would also like to acknowledge the technical support provided by Analytical and Testing Center, Huazhong University of Science and Technology, China. P.K. Wong was also supported by the CAS/SAFEA International Partnership Program for Creative Research Teams of Chinese Academy of Sciences, China.

References

1. D. Venieri, A. Fraggedaki, M. Kostadima, E. Chatzisymeon, V. Binas, A. Zachopoulos, G. Kiriakidis and D. Mantzavinos, *Appl. Catal. B: Environ.*, 2014, **154**, 93.
2. X. Zhong, Z. Dai, F. Qin, J. Li, H. Yang, Z. Lu, Y. Liang and R. Chen, *RSC Adv.*, 2015, **5**, 69312.
3. F. Qin, H. P. Zhao, G. F. Li, H. Yang, J. Li, R. M. Wang, Y. L. Liu, J. C. Hu, H. Z. Sun and R. Chen, *Nanoscale*, 2014, **6**, 5402.
4. Y. H. Lv, C. S. Pan, X. G. Ma, R. L. Zong, X. J. Bai and Y. F. Zhu, *Appl. Catal. B: Environ.*, 2013, **138**, 26.
5. D. Wu, W. Wang, F. T. Tan, F. Z. Sun, H. F. Lu and X. L. Qiao, *RSC Adv.*, 2013, **3**, 20054.
6. L. Nasi, D. Calestani, T. Besagni, P. Ferro, F. Fabbri, F. Licci and R. Mosca, *J. Phys. Chem. C*, 2012, **116**, 6960.
7. Q. Li, B. D. Guo, J. G. Yu, J. R. Ran, B. H. Zhang, H. J. Yan and J. R. Gong, *J. Am. Chem. Soc.*, 2011, **133**, 10878.
8. N. Doss, P. Bernhardt, T. Romero, R. Masson, V. Keller and N. Keller, *Appl. Catal. B: Environ.*, 2014, **154**, 301.
9. Y. Z. Yoo, Z. W. Jin, T. Chikyow, T. Fukumura, M. Kawasaki and H. Koinuma, *Appl. Phys. Lett.*, 2002, **81**, 3798.
10. A. Torabi and V. N. Staroverov, *J. Phys. Chem. Lett.*, 2015, **6**, 2075.
11. E. Kowsari and M. R. Ghezelbash, *Mater. Lett.*, 2011, **65**, 3371.
12. L. F. Hu, M. Chen, W. Z. Shan, T. R. Zhan, M. Y. Liao, X. S. Fang, X. H. Hu and L. M. Wu, *Adv. Mater.*, 2012, **24**, 5872.
13. D. Bao, P. Gao, X. Y. Zhu, S. C. Sun, Y. Wang, X. B. Li, Y. J. Chen, H. Zhou, Y. B. Wang and P. P. Yang, *Chem. Eur. J.*, 2015, **21**, 12728.
14. S. C. Rai, K. Wang, Y. Ding, J. K. Marmon, M. Bhatt, Y. Zhang, W. L. Zhou and Z. L. Wang, *ACS Nano*, 2015, **9**, 6419.
15. J. Lahiri and M. Batzill, *J. Phys. Chem. C*, 2008, **112**, 4304.
16. D. Lehr, M. Luka, M. R. Wagner, M. Bulger, A. Hoffmann and S. Polarz, *Chem. Mater.*, 2012, **24**, 1771.
17. S. K. Pandey, S. Pandey, V. Parashar, R. S. Yadav, G. K. Mehrotra and A. C. Pandey, *Nanoscale*, 2014, **6**, 1602.
18. J. Schrier, D. O. Demchenko and L. W. Wang, *Nano Lett.*, 2007, **7**, 2377.
19. C. Kim, S. J. Doh, S. G. Lee, S. J. Lee and H. Y. Kim, *Appl. Catal. A: Gen.*, 2007, **330**, 127.
20. H. M. Chen, C. K. Chen, R. S. Liu, C. C. Wu, W. S. Chang, K. H. Chen, T. S. Chan, J. F. Lee and D. P. Tsai, *Adv. Energy Mater.*, 2011, **1**, 742.
21. S. K. Pandey, S. Pandey, A. C. Pandey and G. K. Mehrotra, *Appl. Phys. Lett.*, 2013, **102**.
22. Y. X. Li, G. F. Ma, S. Q. Peng, G. X. Lu and S. B. Li, *Appl. Catal. A: Gen.*, 2009, **363**, 180.
23. Z. J. Zhang, W. Z. Wang, J. Ren and J. H. Xu, *Appl. Catal. B: Environ.*, 2012, **123**, 89.
24. K. Dai, L. H. Lu, J. Dong, Z. Y. Ji, G. P. Zhu, Q. Z. Liu, Z. L. Liu, Y. X. Zhang, D. P. Li and C. H. Liang, *Dalton Trans.*, 2013, **42**, 4657.
25. J. M. Khoshman and M. E. Kordesch, *Thin Solid Films*, 2007, **515**, 7393.
26. Y. Cao, H. J. Wang, C. Cao, Y. Y. Sun, L. Yang, B. Q. Wang and J. G. Zhou, *J. Nanopart. Res.*, 2011, **13**, 2759.
27. R. Yi, J. K. Feng, D. P. Lv, M. L. Gordin, S. R. Chen, D. W. Choi and D. H. Wang, *Nano Energy*, 2013, **2**, 498.
28. S. K. Pandey, S. Pandey, A. C. Pandey and G. Mehrotra, *Appl. Phys. Lett.*, 2013, **102**, 233110.
29. I. Shakir, M. Shahid and D. J. Kang, *Chem. Commun.*, 2010, **46**, 4324.
30. D. F. Hou, W. Luo, Y. H. Huang, J. C. Yu and X. L. Hu, *Nanoscale*, 2013, **5**, 2028.
31. J. Wang, Y.-F. Lim and G. W. Ho, *Nanoscale*, 2014, **6**, 9673.

32. H. Ma, J. Han, Y. Fu, Y. Song, C. Yu and X. Dong, *Appl. Catal. B: Environ.*, 2011, **102**, 417.
33. D. Wu, B. Wang, W. Wang, T. An, G. Li, T. W. Ng, H. Y. Yip, C. Xiong, H. K. Lee and P. K. Wong, *J. Mater. Chem. A*, 2015, **3**, 15148.
34. W. Wang, X. Chen, G. Liu, Z. Shen, D. Xia, P. K. Wong and C. Y. Jimmy, *Appl. Catal. B: Environ.*, 2015, **176**, 444.
35. G. C. Huang, D. H. Xia, T. C. An, T. W. Ng, H. Y. Yip, G. Y. Li, H. J. Zhao and P. K. Wong, *Appl. Environ. Microb.*, 2015, **81**, 5174.
36. V. A. Nadtochenko, A. G. Rincon, S. E. Stanca and J. Kiwi, *J. Photochem. Photobiol. A*, 2005, **169**, 131.
37. J. Kiwi and V. Nadtochenko, *Langmuir*, 2005, **21**, 4631.
38. H. Schwegmann, J. Ruppert and F. H. Frimmel, *Water Res.*, 2013, **47**, 1503.
39. X. Nie, G. Y. Li, M. H. Gao, H. W. Sun, X. L. Liu, H. J. Zhao, P. K. Wong and T. C. An, *Appl. Catal. B: Environ.*, 2014, **147**, 562.
40. L. Vojta, D. Caric, V. Cesar, J. A. Dunic, H. Lepedus, M. Kveder and H. Fulgosi, *Sci. Rep.*, 2015, **5**.
41. Y. Noda, S. Murakami, M. Mankura and A. Mori, *J. Clin. Biochem. Nutr.*, 2008, **43**, 185.